Direct observation of competition between charge order and itinerant ferromagnetism in vdW crystal Fe5-xGeTe2

Xuchuan Wu
Renmin University of China
Le Lei
Renmin University of China
Qiangwei Yin
Renmin University of China
Ning-Ning Zhao
Renmin University of China
Man Li
Renmin University of China https://orcid.org/0000-0003-3479-4382
Zilu Wang
Renmin University of China
Qingxin Liu
Renmin University of China
Wenhua Song
Renmin University of China
Huan Ma
Renmin University of China
Pengfei Ding
Renmin University of China https://orcid.org/0000-0001-5869-0030
Kai Liu
Renmin University of China https://orcid.org/0000-0001-6216-333X
Zhihai Cheng
Renmin University of China https://orcid.org/0000-0003-4938-4490
Hechang Lei
Renmin University of China https://orcid.org/0000-0003-0850-8514
Shancai Wang (scw@ruc.edu.cn)
Renmin University of China https://orcid.org/0000-0001-7564-9064

Article

Keywords: ferromagnetism, superconductivity, charge density waves (CDW), magnetism, pseudogap

Posted Date: March 25th, 2021

DOI: https://doi.org/10.21203/rs.3.rs-294909/v1

Direct observation of competition between charge order and itinerant ferromagnetism in vdW crystal $Fe_{5-x}GeTe_2$

Xuchuan Wu,* Le Lei,* Qiangwei Yin,* Ning-Ning Zhao,* Man Li, Zilu Wang, Qingxin Liu, Wenhua Song, Huan Ma, Pengfei Ding, Kai Liu,† Zhihai Cheng,‡ Hechang Lei,§ and Shancai Wang¶
Department of Physics, Beijing Key Laboratory of Optoelectronic Functional Materials & Micro-nano Devices, Renmin University of China, Beijing 100872, China
(Dated: Jan. 21, 2021)

The interplay of symmetry-breaking ordered states, such as superconductivity, charge density waves (CDW), magnetism and pseudogap, is a fundamental issue in correlated system. CDW and antiferromagnetism often coexist in the proximity of phase diagram region in cuprates. It is also worthy nothing that different order states appear in a situation on comparable temperature scales, so these orders are intertwined and competing on the same footing. The magnetism of vdW material $Fe_{5-x}GeTe_2$ with the one of the highest reported bulk Curie temperatures, is found to be sensitive to thermal history and external magnetic field. However, the temperature-dependent magnetization with two characteristic points still lacks a unified picture to describe. Using angle-resolved photoemission spectroscopy, scanning tunneling microscopy, magnetic properties measurements, and the first-principles calculations, the complex yet intriguing magnetic behaviors are gradually unveiled. A competition mechanism between charge order and ferromagnetism is proposed and firmly observed by experimental measurements. As the ferromagnetic order strengthens at low temperature, the charge order will be suppressed. Exchange splitting in itinerant ferromagnetism plays a significant role in the temperature evolution of band structure and causes a Lifshitz transition, which provides more control means to realize novel devices at room temperature.

I. INTRODUCTION

CDW, a periodic modulation of electron density, frequently emerges in high-T_c superconducting materials such as $YBa_2Cu_3O_{7-x}$[1–4] and $La_{2-x}Ba_xCuO_4$[5] and in low-dimensional system[6]. Two-dimensional van der Waals (vdW) crystals with intrinsic magnetism have great potential for the application in spintronic devices and challenges in physics. To date, the demand for versatile performance improvement and efficient information storage in post-silicon electronics have to be settled urgently, and it sparked extensive research in the two-dimensional vdW magnetic materials by combining complementary properties in vdW heterostructure[7].

Intrinsic magnetic vdW materials such as chromium trihalides, CrX_3 (X = Cl, Br, I) and ternary compound Fe_nGeTe_2 have garnered significant attention to their intriguing magnetic properties[8–16]. The ferromagnetic cleavable vdW metal $Fe_{3-x}GeTe_2$ has high Curie temperature T_c = 230 K. More importantly, a room-temperature T_c = 270 ∼ 300K magnet in Fe-Ge-Te compound $Fe_{5-x}GeTe_2$ has been synthesized[17–24]. The cobalt-doped $(Fe_{1-x}Co_x)_5GeTe_2$ has an even higher Curie temperature T_c, stronger magnetic anisotropy and antiferromagnetic state[20, 23], which provide an efficient way to manipulate spintronic device[25–27]. A wide scope of correlation phenomena in 2D materials are also observed, including CDW[28–32], superconductivity[33–36], and Mott insulators[37–39]. They are driven by the factors such as electron correlations, electron-phonon coupling or electronic band topology[9].

The magnetic properties like magnetization are impacted depending on the thermal processing history in $Fe_{5-x}GeTe_2$, which can yield metastable state and distinct stack disorder with a first-order transition at $T \approx$ 110 K[17]. However, a complementary mechanism is still not put forward to explain the complexity of the magnetization curve especially the formation of the order parameter below approximately 165 K. The resistivity drop, ordinary Hall coefficient sign change and the behavior of Seebeck coefficient around 110 K [17, 18] indicate an obvious evolution of electronic band structure and possible change of Fermi surface topologies. These phenomena are intriguing to inspect by more spectroscopic probes.

In this work, by combing the APRES, magnetization measurement, STM, and the first-principles calculation, we firstly illustrate the interplay between band structure, ferromagnetism and charge order in $Fe_{5-x}GeTe_2$. The competition between the itinerant ferromagnetism and charge order is observed in $Fe_{5-x}GeTe_2$, and we provide the first band structure measurement, encountering an electronic symmetry breaking and a Lifshitz transition induced by the magnetic transition coupled with charge order. Exchange splitting in itinerant ferromagnetic model could qualitatively explain the spin-polarized bands shifting, which leads to the carriers change from hole dominance to electron reported in transport measurement[17, 18]. It is revealed by the ARPES measurement together with the first-principles calculation. The periodical modulation $\sqrt{3}a \times \sqrt{3}a$ R30° observed by STM and corresponding features in APRES

* These authors contributed equally.
† kliu@ruc.edu.cn
‡ zhihaicheng@ruc.edu.cn
§ hlei@ruc.edu.cn
¶ SCW@ruc.edu.cn

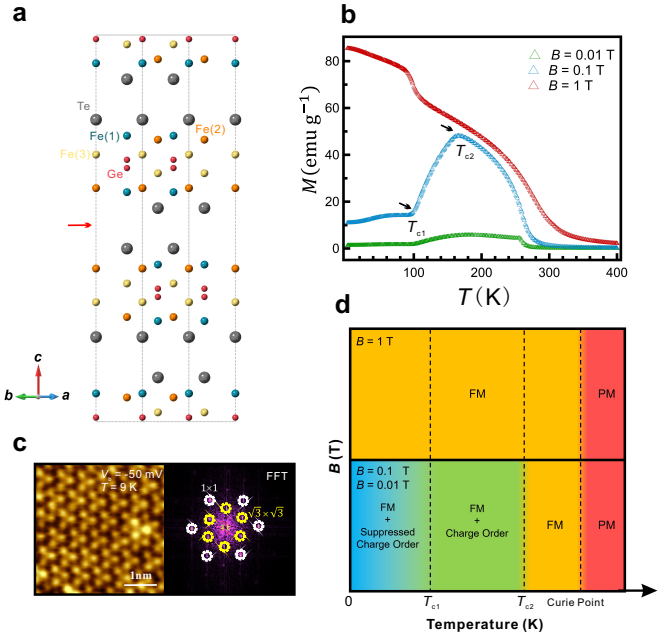

FIG. 1. (a) Schematic of $Fe_{5-x}GeTe_2$ crystal structure with Fe-Ge-Te slab stacked along c-axis, where Fe(1) and Ge are split sites that allow for local atomic order and disorder. (b) Temperature-dependent magnetization curves for $H \parallel ab$ at different field indicated by the colors. (c) Atomic-resolution STM image and the corresponding Fast Fourier Transform (FFT) image of $Fe_{5-x}GeTe_2$ surface (V_b = -50 mV, I_t= -100 pA, T = 9 K), where vdW gap is the cleavage plane. The white and yellow dotted circles in the FFT image indicate the 1×1 and $\sqrt{3}a\times\sqrt{3}a$ R30° structures, respectively. (d) Phase diagram of $Fe_{5-x}GeTe_2$ crystal in different magnetic fields.

measurement at two characteristic temperature points can be interpreted by the temperature-dependent competitive mechanism well.

II. RESULTS

Fig. 1a shows schematic of the average crystal structure determined by single crystal X-ray diffraction (XRD) pattern. The Fe-Ge sublayers stack along c direction in the centrosymmetric space group $R\bar{3}m$ (No. 166) with a = 4.0375(5) Å and c = 29.191(1) Å by Rietveld refinement. The cleavage plane oriented along the c axis is marked by the red arrow, due to the adjacent Te layers connected by weak vdW interaction. The vacancy of Fe and the tendency to form atomic short-range order/disorder lead to an uncertain x in $Fe_{5-x}GeTe_2$. The Fe vacancies are identified as $Fe_{4.78(4)}GeTe_{2.13(1)}$, when setting the content of Ge as 1 derived from XRD pattern and the energy-dispersive X-ray (EDX) spectrum. The Fe(1) and Ge are split sites, where Fe(1) can be above or below the neighboring Ge, or can be vacant.

The magnetization $M(T)$ for B = 0.01 T, 0.1 T and 1 T along ab plane are shown in Fig. 1b. The magnetization curves clearly exhibit the FM transition at approximately 300 K. It shows two clear transitions at $T_{c2} \approx$ 165 K (B = 0.01 T at $T_{c2} \approx$ 180 K) and $T_{c1} \approx$ 110 K successively below Curie temperature, marked by the black arrows. When cooling below T_{c2} at low field B = 0.01 T or B = 0.1 T, the $M(T)$ curves start to decline, but the one at B = 1 T rises. An order parameter is formed at T_{c2} and compete with the magnetism, and it can be suppressed under a relatively large magnetic field at B = 1 T. The superstructure modulation vector $\boldsymbol{q}$ = (1/3, 1/3, 1) has been revealed by the selected-area electron diffraction above T = 100 K, and fades below 100 K[18]. The atomic-resolution STM images in Fig. 1c show a clear trimerization of the atoms (V_b = -50 mV, T = 9 K). The FFT image can distinguish the $\sqrt{3}a\times\sqrt{3}a$ R30° periodic modulation induced by the charge order and the primitive 1×1 structure simultaneously. The corresponding impacts on electronic band structure caused by the charge order will be discussed later. When the temperature continuously drops below T_{c1}, upturn points of the $M(T)$ curves are distinguished at all magnetic field in Fig. 1b. Albeit no consensus has been reached on the mechanism of the transition at T_{c1} [17, 40], the reduced rate of descent at low field B = 0.01 T or B = 0.1 T and the continuous increase at B = 1 T of the magnetization curves support the enhancement of the ferromagnetic order. Consequently, the enhancement will clearly affect the competitive situation between the charge order and ferromagnetism.

Fig. 2 shows the electronic band structures and DFT calculations of $Fe_{5-x}GeTe_2$ in the magnetic state at low temperature T = 30 K where the charge order is suppressed and the magnetic anisotropy tends to support easy-axis along c-axis[17, 22, 40]. As shown in Fig. 2a and 2b, the Fermi surface (FS) contour at low temperature T = 30 K consists of a circular (α) and a hexagonal (β) hole pockets centered at the Γ point, a nearly triangular electron pocket (γ) around at the K point and a small electron pocket (δ) at the M point. The DFT calculated FS with chemical component at x = 0.33 ($Fe_{4.67}GeTe_2$) (see Methods for the DFT details) is consistent with the experimental crystal x = 0.22 ($Fe_{4.78}GeTe_2$) determined by EDX. Despite of the matrix element effect, the FS topology conforms more with the C_6 rotational symmetry at low temperature, which meets the expectation from the calculated FS (Fig. 2b).

We have further verified the consistency between the experimental ARPES results (Fig. 2e-h) and the calculated band structure (Fig. 2c) along the high symmetry lines with the magnetization along c-axis. In addition, the DFT calculation with magnetization in ab-plane is also performed (see Fig. s1 in the Supplementary). Both show the major hole bands (α, β) and electron bands (γ at K, δ at M). A careful comparison between the DFT calculations and the ARPES intensity maps (the second derivative) along the high symmetry lines also reveals that the DFT calculations ($Fe_{4.67}GeTe_2$) with magnetization along c-axis agree well with the experimental

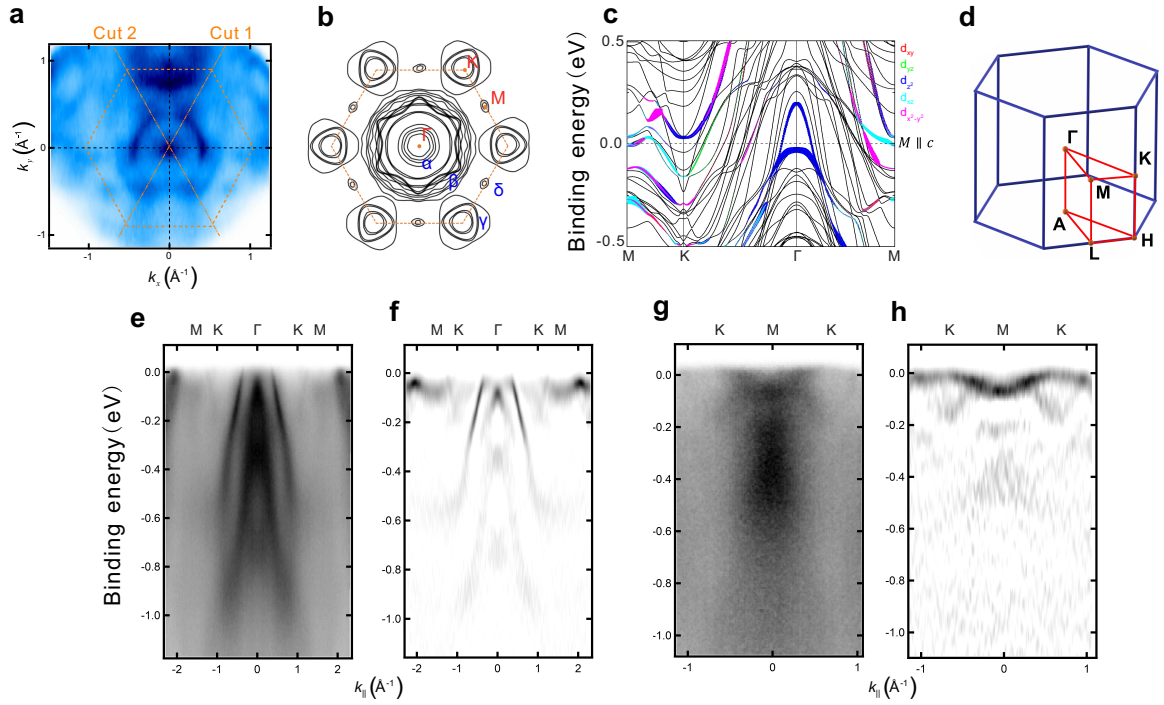

FIG. 2. **ARPES band mapping at 30 K and DFT band calculations for $Fe_{5-x}GeTe_2$.** (a) Photoemission intensity map at the E_F in k_x-k_y plane at 30 K, and the orange hexagon indicates the Brillouin zone (BZ) boundary. The ARPES spectra taken on a nearly stoichiometric single crystal of $Fe_{5-x}GeTe_2$ ($x = 0.22$) (b) The calculated FSs at $k_z = 0$ plane and the high-symmetry points are presented in (d). (c) The calculated band structures along the high symmetry lines, and the magnetic moments are given by $M \parallel c$. The calculated Fe $3d$ orbital contributions is imposed on (c). (d) The BZ of $Fe_{5-x}GeTe_2$ with the high symmetry points and lines indicated. (e)(f) and (g)(h) The photoemission intensity and their second derivative of the intensity plots along the Γ-K-M direction and the K-M-K direction, respectively.

results at low temperature $T = 30$ K. From the photoemission intensity plot along the Γ-K-M (Fig. 2e-f), there are only hole-like bands around the Γ point and electron-like pockets around the M/K point near the Fermi level, respectively. It is noteworthy that the electron-like band δ is located at the 100 meV below E_F and shows a relatively large effective electron mass, which can induce relatively high density of states and influence the Hall conductance.

To understand the behavior of temperature-dependent magnetization and its competition with charge order, we explore the temperature evolution of the band structure and show them in Fig. 3. When the temperature drops to 150 K, the FS contour displays a prominent C_3 rotational symmetry centered at Γ. The rotational symmetry of FS is broken from C_6 to C_3 due to the $\sqrt{3}a \times \sqrt{3}a$ R30° periodic modulation induced by charge order (see Fig. s2 in the Supplementary for details). The photoemission intensity plots along the two high symmetry lines of adjacent $\frac{\pi}{3}$, Cut 3 (Fig. 3b) and Cut 4 (Fig. 3c), confirm that the morphology of the hole-like pockets β have distorted compared with the experimental and calculated FS at the low temperature $T = 30$ K (see Fig. s3 in the Supplementary for details).

Along the Γ-K-M direction, a continuous slow cooling process (Fig. 3d-j) was performed carefully. A shallow electron-like band originating from the $\sqrt{3}a \times \sqrt{3}a$ R30° charge order is observed (the band γ^* marked by red arrow), which is discussed in detail in Fig. 5. It persists above T_{c1} and gradually fades with the decrease of temperature below T_{c1}. The enhanced magnetic order below T_{c1} suppresses the charge order, resulting in a weakening band folding feature and the recovery of the FS rotational symmetry from C_3 to C_6. The temperature-dependent momentum distribution curves (MDCs) of the band β are extracted along the Γ-K-M direction at binding energy -200 meV, as show in Fig. 3k. The peak width of the MDCs starts to decrease when cooling below T_{c1}, and the MDC width is proportional to the inverse of the mean free path of quasi-particles (QPs) scattering in ARPES measurements.

For an itinerant magnetic system, there is normally a shift of the band with the change of the magnetization. The temperature-dependent core level spectra (Fig. 4a) obviously exhibit Fe $3p_{3/2}$, Te $4d_{3/2}$, Te $4d_{5/2}$, Ge $3d_{3/2}$ and Ge $3d_{3/2}$ core level peaks, in which no peak shift is distinguished, and the sharp characteristic peaks confirm the chemical composition of $Fe_{5-x}GeTe_2$ compound. It rules out the possibility that the transition point T_{c1} derives from the change of chemical valence in Fe atoms. While the neutron power diffraction measurement reported slight change of lattice parameters less than 0.1%

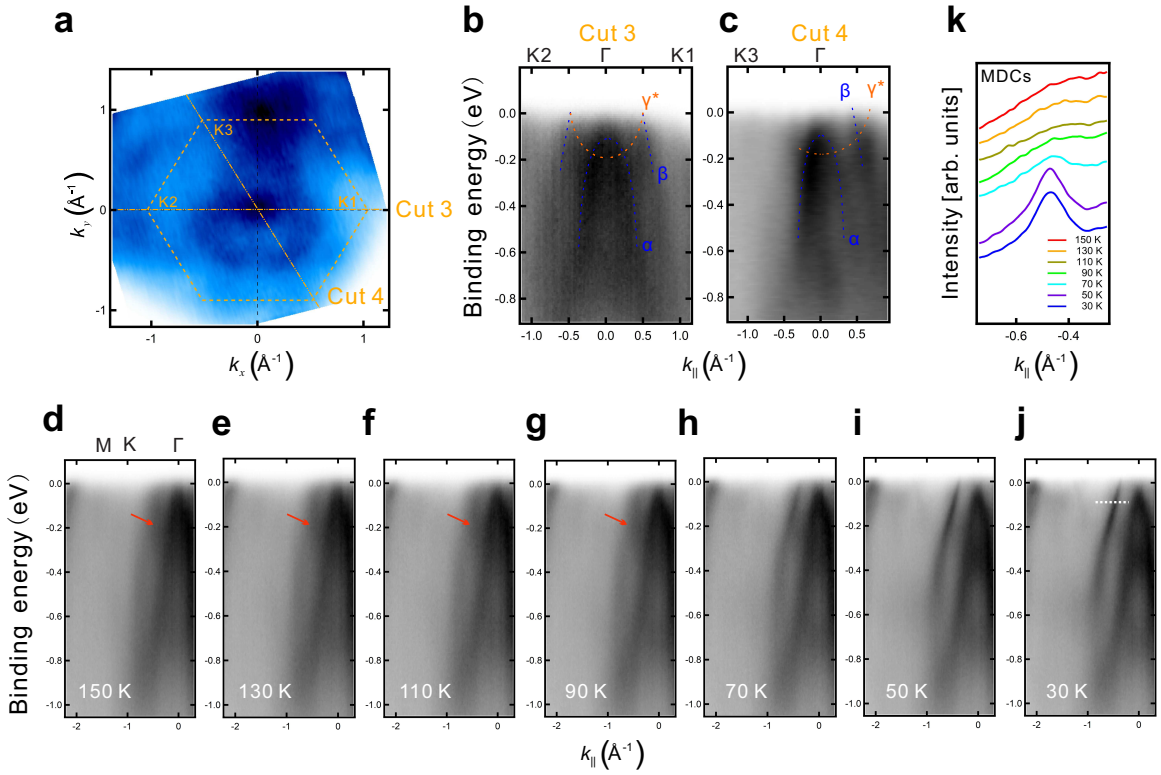

FIG. 3. **Temperature-dependence of the band structure.** (a) Photoemission intensity map at E_F in k_x-k_y plane at 150 K. (b)(c) The intensity maps along the cut 3 and cut 4 indicated in (a), and the shallow electron-like band feature originated from the charge order is labeled γ^*. (d-j) Temperature dependence of the band structure along the Γ-K-M direction from T = 150 K to 30 K. The electron-like band γ^* is indicated by the red arrows. (k) Temperature-dependent MDCs extracted from (d-j) at the binding energy -0.1 eV, indicated by the dash line in (j).

at T_{c1}[21], the electronic structure changes near E_F are unlikely from crystal structural origin.

To characterize how the bands evolve with the decrease of temperature, we show the detailed temperature-dependent energy distribution curves (EDCs) taken at the BZ center Γ (Fig. 4b). Upon cooling, the spectral weight at about -400 meV binding energy (indicated by the gray shaded area in Fig. 4b) increase rapidly about T_{c1}, and down to low temperature (see Supplementary Fig. s4 for the EDCs at different temperature). At the same time, the peak at -120 meV sharpens and continuously moves toward E_F with the decrease of temperature. In contrast to the position indicated by black arrow in Fig. 4b at T = 150 K, the extracted energy position reduced from 120 meV to 78 meV relative to E_F (Fig. 4c). It is recognized as a charge order induced gap feature shown in Fig. 3. The enhancement of the ferromagnetic order suppresses the charge order when cooling through T_{c1} and leads to a reduction of the gap.

The temperature evolution of EDCs at the point M shows that a small electron pocket shifts down below the E_F around T_{c1} (indicated by the back arrow in Fig. 4d). The band structure calculations reveal that the hole-like bands around Γ and electron-like bands around M are all spin-polarized (see Fig. s1 in the Supplementary). The electron-like band at M are consistent with itinerant ferromagnetism characteristic. It is also supported by the calculated spin-polarized density of states on Fe atoms shown in (Fig. s5 in Supplementary). The downwards movement of the electron-like band at M, thus the formation of an electron-like pocket, can cause the carrier sign change and Lifshitz transition when cooling below T_{c1}.

III. DISCUSSION

Prior studies have noted that a $\sqrt{3}a \times \sqrt{3}a$ R30° short-range order reflected by the FFT pattern of the high-angle annular dark field (HAADF) image[21] along [1$\bar{1}$0]. The corresponding periodic modulation was also observed by the selected-area electron diffraction[18]. In this paper, STM and ARPES unambiguously confirm the $\sqrt{3}a \times \sqrt{3}a$ R30° periodic modulation both in real space and reciprocal space . From the $M(T)$ curves in Fig. 1b, the periodical modulation forms at T_{c2}, where the magnetization encounters a sudden drop in weak external magnetic fields (B = 0.01 T and B = 0.1 T). Relatively strong external magnetic field (B = 1 T) suppresses this periodic modulation. The aforementioned evidences

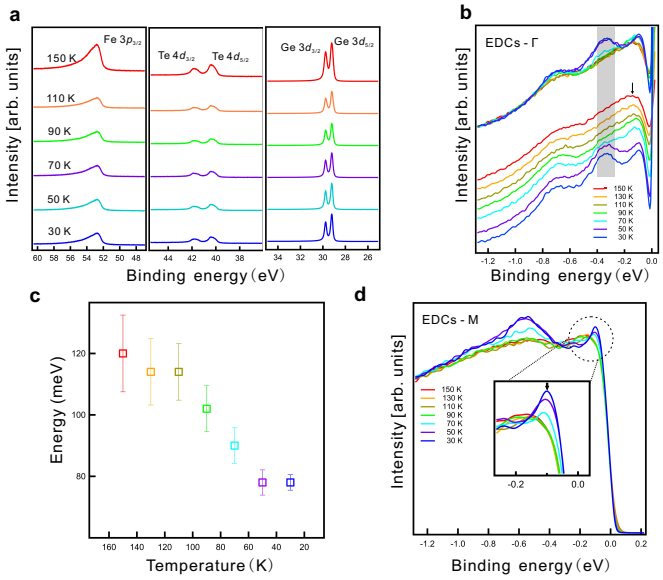

FIG. 4. **Temperature dependence of the EDC peaks.** (a) ARPES core level spectrum shows clear Fe $3p$, Te $4d$ and Ge $3d$ peaks with the decrease of temperature at $h\nu = 200$eV. (b) Temperature dependence of the EDCs at Γ divided by Fermi-Dirac distribution function. (c) The energy gap defined as the peak positions indicated by the black arrow in (b) at the corresponding temperature. The thermal fluctuation is indicated by the error bars. (d) Temperature dependence of the normalized EDCs at M, and the temperature-dependent shift of the peaks indicated by the black arrow nearing the E_F is magnified.

show that the enhancement of the ferromagnetic order cooling below T_{c1} weakens the charge order.

A $\sqrt{3}a \times \sqrt{3}a$ R30° periodic modulation is proposed to inspect this order viewed by previous electron diffraction pattern, STM, and APRES results. The corresponding reciprocal space of superlattice is imposed on the primitive BZ (Fig. 5b). The K point in the superlattice BZ coincides with Γ in the primitive BZ, and the electron-like band dispersion at K is folded back to Γ, which is obviously detected, shown as γ^* in Fig. 3b-j. Furthermore, the folded electron-like band gradually vanishes when the temperature decreases especially through T_{c1}, which supports the suppression of the charge order state by the enhanced ferromagnetism. The presence of $\sqrt{3}a \times \sqrt{3}a$ R30° periodic modulation will result in the rotational symmetry breaking from C_6 to C_3, and it partially restores to C_6 rotational symmetry when cooling to $T = 30$ K. Comparing the FS at $T = 150$ K and 30 K, the FS evolves from a three-petal to hexagonal shape.

The magnetic anisotropy properties in the Fe_nGeTe_2 family ferromagnets are manifested by the low temperature. An approximate temperature transition at $T \approx 110$ K has been reported in Fe_4GeTe_2, in which the easy-plane anisotropy reorients to the easy-axis anisotropy when cooling through the critical temperature driven by the small effective uniaxial magnetic anisotropy[40]. Moreover, it is reported that the Fe at the different locations become in FM order at different temperature[17]. Previous studies show a first-order magnetostructural transition due to the FM order of Fe(1) below T_{c1} by Mössbauer spectral and neutron diffraction[21]. Cobalt substation experiment on the composition $Fe_{5-y}Co_yGeTe_2$ at $y = 0.2$ shows that the transition at T_{c1} in $M(T)$ and $R(T)$ curves disappear[22]. Besides, the corresponding DFT calculation approves that the dopants preferentially occupy the Fe(1) sites at $y = 0.2$[20]. Despite the ambiguity of the mechanism, they both approved the enhancement of the ferromagnetic order when cooling through T_{c1}. The enhancement of FM suppresses the charge order below T_{c1} and causes the C_6 rotational symmetry recovery of the FS. Additionally, the band folding feature induced by the charge order fades. Previous transport studies in the rare earth element compound polycrystals and the first-principles calculation on monolayer $NbSe_2$ propose that the FM state could suppress the CDW state and restore the effects on FS caused by CDW[41, 42]. The temperature dependence of energy gap extracted from the EDCs at Γ in Fig. 4c shows 50 meV decrease, which also supports the competition mechanism between the charge order and FM. The magnetoelastic effect was previously observed around $T = 110$ K via neutron power diffraction probably caused by changes in the electronic structure[17]. The lattice parameter a increases and the c decreases upon cooling through T_{c1}, which can also weaken the charge order. In addition, the inverse mobility can be calculated by the formula $\mu^{-1} = m^*\nu_F/e\tau\nu_F = \hbar k_F \Delta k/e$, where Δk is the MDC width[43]. The abrupt decrease of resistivity at T_{c1} can be partially explained by the sudden decrease of QP scattering caused by the enhanced magnetic order at Fe(1)[21] and the suppression of charge order.

For a FM metal, the electronic bands split below Curie temperature with long-range order[44]. The spectral weight transfer in the FM state in $Fe_{3-x}GeTe_2$ and the sensitive response of the anomalous Hall effect to the magnetic transition have demonstrated that the itinerant ferromagnetic mechanism is involved in the evolution of the electronic structure among the Fe-Ge-Te family[8, 40]. With the decrease of temperature and the enhancement of the ferromagnetic order, the spin-exchange splitting between the spin-polarized bands increases. The relatively flat spin-polarized electron-like band δ at the M point shifts down below E_F when cooling through T_{c1} (Fig. 4d), which causes the sign change of Hall coefficient and the sharp decrease of Seebeck coefficient[17, 18].

The charge order opens a gap to reduce the density of electron states at E_F, and there is a positive correlation between the susceptibility and the density of states at E_F. In Stoner model, $\chi = \mu_B^2 \frac{N(E_F)}{1-\frac{UN(E_F)}{2}}$, $N(E_F)$ and U are the density of states at Fermi level and the electron interaction between the spin-up and spin-down, respectively.

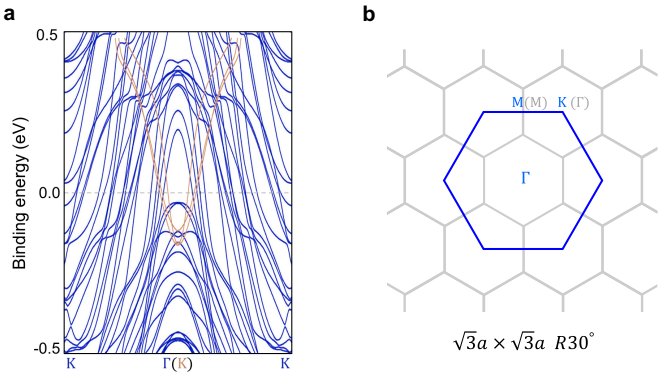

FIG. 5. **Band folding along the K-Γ-K in $Fe_{5-x}GeTe_2$ and the reconstruction of Brillouin zone.** (a) The band dispersion obtained from DFT calculation along the high symmetry line K-Γ-K with the moments $M \parallel c$, and the band along the Γ-K from the charge order are superimposed, indicated by the orange lines. (b) The blue and gray hexagons represent the BZ of the primitive cell and superlattice of $\sqrt{3}a \times \sqrt{3}a$ R30° periodicity, respectively.

In this material, the charge order and the itinerate ferromagnetism are competing for the electron density near E_F and drive the successive transitions at T_{c2} and T_{c1}. Here we establish a unified image to depict the magnetization curves, STM and ARPES experiments.

IV. CONCLUSIONS

In summary, we perform ARPES, STM, magnetization measurement, and the first-principles calculation to elaborate the behaviors at two critical temperatures T_{c1} and T_{c2} in vdW ferromagnetic material $Fe_{5-x}GeTe_2$. The temperature plays a significant role in driving the competitive evolution between the charge order and the itinerant ferromagnetism, in which the electronic band structure evolution is coupled to the charge order and itinerant ferromagnetic by band folding and spin-exchange splitting. The complex magnetic transport properties in $Fe_{5-x}GeTe_2$ also attribute to the disorder influenced by heat treatment history of the sample, which confirms the relatively weak thermal stability in the vdW-type Fe_nGeTe_2 compounds[40]. In this work, we provide the first direct observation of the temperature driven competition between the charge order and the ferromagnetism.

The relative dominance between the charge order and ferromagnetism can be controlled by either external magnetic magnitude or temperature. It is foreseeable that the equilibrium of the order states can be perturbed easily in $Fe_{5-x}GeTe_2$. As a result, resistivity, Hall coefficient, and anisotropy induced by symmetry breaking can be tuned by broad means, such as gating, strain, and heterostructures. These rich control ways open a door to switching phenomena in spintronic devices. Theoretically, it is favorable to understand the coexistence and competition among the various orders in correlated systems like high-T_c superconductors.

V. METHODS

First-principles calculations

The first-principles electronic structure calculations on $Fe_{5-x}GeTe_2$ were performed with the projector augmented wave (PAW) method[45] as implemented in the Vienna Ab Initio Simulation Package (VASP)[46]. The generalized gradient approximation (GGA) of Perdew-Burke-Ernzerhof (PBE)[47] type was adopted for the exchange-correlation functional. The kinetic energy cutoff of the plane-wave basis was set to 400 eV. A $15\times15\times2$ k-point mesh was used for the BZ sampling. The lattice constants were fixed to the experimental values ($a = b = 4.044$ Å, $c = 29.247$ Å)[21] and the internal atomic positions were fully relaxed until the forces on all atoms were smaller than 0.01 eV/ Å. To simulate $Fe_{5-x}GeTe_2$ with Fe vacancies, we have symmetrically deleted four Fe atoms at the Fe(1) sites from the Fe_6GeTe_2 cell that contains three formula units, which results in a chemical component of $Fe_{4.67}GeTe_2$. The spin-orbit coupling (SOC) effect was included in the band structure calculations. The two-dimensional (2D) FSs were calculated based on the tight-binding Hamiltonian constructed with the maximally localized Wannier functions [48, 49] for the outmost s and d orbitals of Fe atom, s, p, and d orbitals of Ge atom, and s and p orbitals of Te atom generated by the first-principles calculations.

ARPES measurements

ARPES measurements were performed at the Dreamline beamline of the Shanghai Synchrotron Radiation Facility (SSRF) using a Scienta D80 analyzer and the BL13U beamline in National Synchrotron Radiation Laboratory (NSRL) in Heifei. The overall energy and angular resolutions were set better than 25 meV and 0.2°, respectively. The sample were cleaved in situ along the (001) plane and measured under ultrahigh vacuum better than 4×10^{-11} mbar. The sample was cooled using an average ramp rate of 1 K/min from 160 K to 30 K (excluding the data collection process), ensuring the sample was quenched but not cooled below the first-order transition ($T_{c1} = 110$ K).

Scanning tunneling microscopy

The samples used in the experiments were cleaved in situ in ultra-high vacuum chamber, and then immediately transferred to the STM head. STM experiments were performed with LT-STM (PanScan Freedom, RHK). The low temperature STM measurements were performed at 9 K with chemical etched W tip. All STM images were processed by software Gwyddion.

Sample synthesis, structure, magnetization and composition characterization

Single crystals of $Fe_{5-x}GeTe_2$ were grown through the

chemical vapor transport method with iodine as transport agent. High-purity Fe (powder), Ge (powder), and Te (grain) were taken in a stoichiometric molar ratio of 5:1:2 and placed in an evacuated tube together with 50 mg of iodine. The tube was heated to 1050 ℃ for 10 h and the temperature was maintained for 6 h; it was then cooled to 760 ℃ at a rate of 5 ℃ h^{-1}, and the temperature was maintained for 50 h and then quenched. Shiny crystals with typical sizes of approximately $3 \times 2 \times 0.05$ mm^3 (length × width × thickness) were obtained. Single crystal XRD pattern were acquired using a Bruker D8 X-ray diffractometer with Cu K_α radiation ($\lambda = 0.15418$ nm) at room temperature of 298 K. The elemental analysis was performed using EDX spectroscopy analysis in a FEI Nano 450 Scanning electron microscope.The magnetization measurements were performed using a Quantum Design MPMS3.

ACKNOWLEDGMENTS

This work was supported by the National Natural Science Foundation of China (Grant No. 11774421, 11774424, 11774423, 11822412, 61674045), the National Key R&D Program of China (Grant No. 2017YFA0302903, 2018YFE0202600, 2016YFA0300504), the Beijing Natural Science Foundation (Grant No. Z200005), the CAS Interdisciplinary Innovation Team, the Fundamental Research Funds for the Central Universities, the Ministry of Science and Technology (MOST) of China (No. 2016YFA0200700), the Strategic Priority Research Program (Chinese Academy of Sciences, CAS) (No. XDB30000000), and the Research Funds of Renmin University of China (Grant No. 19XNLG13, 18XNLG14, 19XNLG17). Computational resources were provided by the Physical Laboratory of High-Performance Computing at Renmin University of China.

Author contributions

X.W. and S.W. carried out the ARPES measurements. Q.Y. and H.L. synthesized the single crystal and performed magnetism and structure measurements. L.L and Z.C carried out the STM measurements. N.Z and K.L performed the first-principles calculations. X.W and S.W. co-wrote the paper and all authors contributed to discussions about and the preparation of the manuscript.

Competing financial interests

The authors declare no competing financial interests.

[1] T. Wu, H. Mayaffre, S. Kramer, M. Horvatic, C. Berthier, W. N. Hardy, R. Liang, D. A. Bonn, and M. H. Julien, Nat Commun **6**, 6438 (2015).
[2] A. J. Achkar, R. Sutarto, X. Mao, F. He, A. Frano, S. Blanco-Canosa, M. Le Tacon, G. Ghiringhelli, L. Braicovich, M. Minola, M. M. Sala, C. Mazzoli, R. Liang, D. A. Bonn, W. N. Hardy, B. Keimer, G. A. Sawatzky, and D. G. Hawthorn, Phys Rev Lett **109**, 167001 (2012).
[3] G. Ghiringhelli, M. Le Tacon, M. Minola, S. Blanco-Canosa, C. Mazzoli, N. B. Brookes, G. M. De Luca, A. Frano, D. G. Hawthorn, F. He, T. Loew, M. Moretti Sala, D. C. Peets, M. Salluzzo, E. Schierle, R. Sutarto, G. A. Sawatzky, E. Weschke, B. Keimer, and L. Braicovich, Science **337**, 821 (2012).
[4] J. Chang, E. Blackburn, A. T. Holmes, N. B. Christensen, J. Larsen, J. Mesot, R. Liang, D. A. Bonn, W. N. Hardy, A. Watenphul, M. v. Zimmermann, E. M. Forgan, and S. M. Hayden, Nature Physics **8**, 871 (2012).
[5] M. Fujita, H. Goka, K. Yamada, J. M. Tranquada, and L. P. Regnault, Physical Review B **70**, 10.1103/PhysRevB.70.104517 (2004).
[6] D. E. Moncton, J. D. Axe, and F. J. DiSalvo, Physical Review B **16**, 801 (1977).
[7] A. K. Geim and I. V. Grigorieva, Nature **499**, 419 (2013).
[8] Y. Zhang, H. Lu, X. Zhu, S. Tan, W. Feng, Q. Liu, W. Zhang, Q. Chen, Y. Liu, X. Luo, D. Xie, L. Luo, Z. Zhang, and X. Lai, Sci Adv **4**, eaao6791 (2018).
[9] K. Kim, J. Seo, E. Lee, K. T. Ko, B. S. Kim, B. G. Jang, J. M. Ok, J. Lee, Y. J. Jo, W. Kang, J. H. Shim, C. Kim, H. W. Yeom, B. Il Min, B. J. Yang, and J. S. Kim, Nat Mater **17**, 794 (2018).
[10] M. A. McGuire, H. Dixit, V. R. Cooper, and B. C. Sales, Chemistry of Materials **27**, 612 (2015).
[11] I. Tsubokawa, Journal of the Physical Society of Japan **15**, 1664 (1960).
[12] M. A. McGuire, G. Clark, S. Kc, W. M. Chance, G. E. Jellison, V. R. Cooper, X. Xu, and B. C. Sales, Physical Review Materials **1**, 10.1103/PhysRevMaterials.1.014001 (2017).
[13] B. Huang, G. Clark, E. Navarro-Moratalla, D. R. Klein, R. Cheng, K. L. Seyler, D. Zhong, E. Schmidgall, M. A. McGuire, D. H. Cobden, W. Yao, D. Xiao, P. Jarillo-Herrero, and X. Xu, Nature **546**, 270 (2017).
[14] Z. Fei, B. Huang, P. Malinowski, W. Wang, T. Song, J. Sanchez, W. Yao, D. Xiao, X. Zhu, A. F. May, W. Wu, D. H. Cobden, J. H. Chu, and X. Xu, Nat Mater **17**, 778 (2018).
[15] Y. Deng, Y. Yu, Y. Song, J. Zhang, N. Z. Wang, Z. Sun, Y. Yi, Y. Z. Wu, S. Wu, J. Zhu, J. Wang, X. H. Chen, and Y. Zhang, Nature **563**, 94 (2018).
[16] B. Chen, J. Yang, H. Wang, M. Imai, H. Ohta, C. Michioka, K. Yoshimura, and M. Fang, Journal of the Physical Society of Japan **82**, 10.7566/jpsj.82.124711 (2013).
[17] A. F. May, C. A. Bridges, and M. A. McGuire, Physical Review Materials **3**, 10.1103/PhysRevMaterials.3.104401 (2019).
[18] Y. Gao, Q. Yin, Q. Wang, Z. Li, J. Cai, T. Zhao, H. Lei, S. Wang, Y. Zhang, and B. Shen, Adv Mater **32**, e2005228 (2020).
[19] H. Zhang, R. Chen, K. Zhai, X. Chen, L. Caretta, X. Huang, R. V. Chopdekar, J. Cao, J. Sun, J. Yao, R. Birgeneau, and R. Ramesh, Physical Review B **102**, 10.1103/PhysRevB.102.064417 (2020).

[20] C. Tian, F. Pan, S. Xu, K. Ai, T. Xia, and P. Cheng, Applied Physics Letters **116**, 10.1063/5.0006337 (2020).

[21] A. F. May, D. Ovchinnikov, Q. Zheng, R. Hermann, S. Calder, B. Huang, Z. Fei, Y. Liu, X. Xu, and M. A. McGuire, ACS Nano **13**, 4436 (2019).

[22] A. F. May, M.-H. Du, V. R. Cooper, and M. A. McGuire, Physical Review Materials **4**, 10.1103/PhysRevMaterials.4.074008 (2020).

[23] J. Stahl, E. Shlaen, and D. Johrendt, Zeitschrift für anorganische und allgemeine Chemie **644**, 1923 (2018).

[24] M. Joe, U. Yang, and C. Lee, Nano Materials Science **1**, 299 (2019).

[25] S. Jiang, J. Shan, and K. F. Mak, Nat Mater **17**, 406 (2018).

[26] S. Jiang, L. Li, Z. Wang, K. F. Mak, and J. Shan, Nat Nanotechnol **13**, 549 (2018).

[27] D. MacNeill, G. M. Stiehl, M. H. D. Guimaraes, R. A. Buhrman, J. Park, and D. C. Ralph, Nature Physics **13**, 300 (2016).

[28] S. V. Borisenko, A. A. Kordyuk, A. N. Yaresko, V. B. Zabolotnyy, D. S. Inosov, R. Schuster, B. Buchner, R. Weber, R. Follath, L. Patthey, and H. Berger, Phys Rev Lett **100**, 196402 (2008).

[29] M. Johannes, I. Mazin, and C. Howells, Physical Review B **73**, 10.1103/PhysRevB.73.205102 (2006).

[30] K. Tsutsumi, Physical Review B **26**, 5756 (1982).

[31] L. Bawden, S. P. Cooil, F. Mazzola, J. M. Riley, L. J. Collins-McIntyre, V. Sunko, K. W. Hunvik, M. Leandersson, C. M. Polley, T. Balasubramanian, T. K. Kim, M. Hoesch, J. W. Wells, G. Balakrishnan, M. S. Bahramy, and P. D. King, Nat Commun **7**, 11711 (2016).

[32] J. A. Wilson, F. J. Di Salvo, and S. Mahajan, Physical Review Letters **32**, 882 (1974).

[33] D. J. Rahn, S. Hellmann, M. Kalläne, C. Sohrt, T. K. Kim, L. Kipp, and K. Rossnagel, Physical Review B **85**, 10.1103/PhysRevB.85.224532 (2012).

[34] E. Morosan, H. W. Zandbergen, B. S. Dennis, J. W. G. Bos, Y. Onose, T. Klimczuk, A. P. Ramirez, N. P. Ong, and R. J. Cava, Nature Physics **2**, 544 (2006).

[35] L. J. Li, E. C. O'Farrell, K. P. Loh, G. Eda, B. Ozyilmaz, and A. H. Castro Neto, Nature **529**, 185 (2016).

[36] T. Kiss, T. Yokoya, A. Chainani, S. Shin, T. Hanaguri, M. Nohara, and H. Takagi, Nature Physics **3**, 720 (2007).

[37] F. Zwick, H. Berger, I. Vobornik, G. Margaritondo, L. Forró, C. Beeli, M. Onellion, G. Panaccione, A. Taleb-Ibrahimi, and M. Grioni, Physical Review Letters **81**, 1058 (1998).

[38] J. J. Kim, W. Yamaguchi, T. Hasegawa, and K. Kitazawa, Phys Rev Lett **73**, 2103 (1994).

[39] J. A. Wilson, F. J. Di Salvo, and S. Mahajan, Advances in Physics **24**, 117 (1975).

[40] J. Seo, D. Y. Kim, E. S. An, K. Kim, G.-Y. Kim, S.-Y. Hwang, D. W. Kim, B. G. Jang, H. Kim, G. Eom, S. Y. Seo, R. Stania, M. Muntwiler, J. Lee, K. Watanabe, T. Taniguchi, Y. J. Jo, J. Lee, B. I. Min, M. H. Jo, H. W. Yeom, S.-Y. Choi, J. H. Shim, and J. S. Kim, Science Advances **6**, 10.1126/sciadv.aay8912 (2020).

[41] F. Zheng, Z. Zhou, X. Liu, and J. Feng, Physical Review B **97**, 10.1103/PhysRevB.97.081101 (2018).

[42] H. Lei, K. Wang, and C. Petrovic, J Phys Condens Matter **29**, 075602 (2017).

[43] T. Yoshida, S. Komiya, X. J. Zhou, K. Tanaka, A. Fujimori, Z. Hussain, Z. X. Shen, Y. Ando, H. Eisaki, and S. Uchida, Physical Review B **80**, 10.1103/PhysRevB.80.245113 (2009).

[44] E. C. Stoner, The London, Edinburgh, and Dublin Philosophical Magazine and Journal of Science **15**, 1018 (2009).

[45] P. E. Blochl, Phys Rev B Condens Matter **50**, 17953 (1994).

[46] G. Kresse and J. Furthmüller, Computational Materials Science **6**, 15 (1996).

[47] J. P. Perdew, K. Burke, and M. Ernzerhof, Phys Rev Lett **77**, 3865 (1996).

[48] N. Marzari, A. A. Mostofi, J. R. Yates, I. Souza, and D. Vanderbilt, Reviews of Modern Physics **84**, 1419 (2012).

[49] A. A. Mostofi, J. R. Yates, G. Pizzi, Y.-S. Lee, I. Souza, D. Vanderbilt, and N. Marzari, Computer Physics Communications **185**, 2309 (2014).

Figures

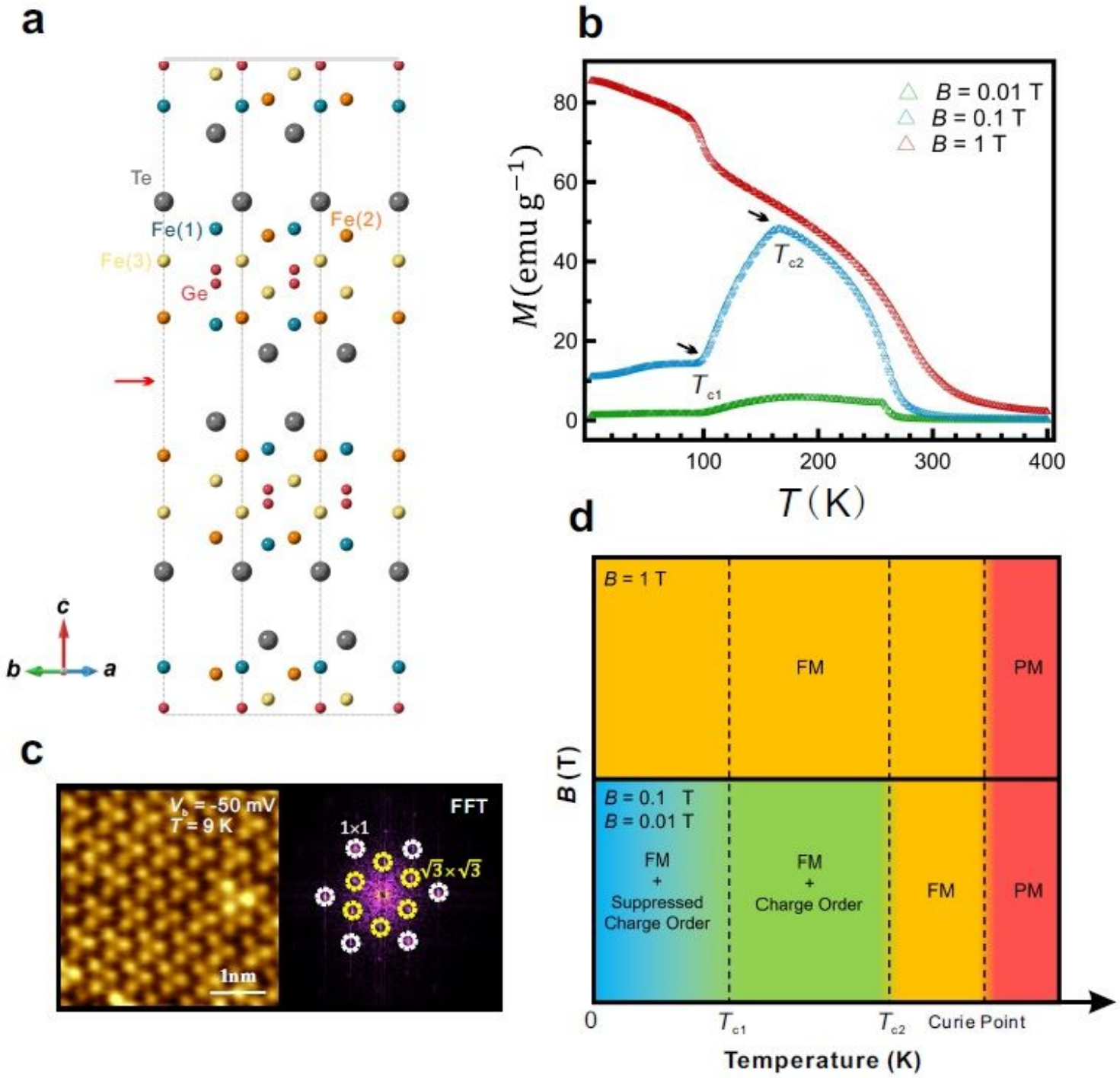

Figure 1

(see Manuscript file for figure legend)

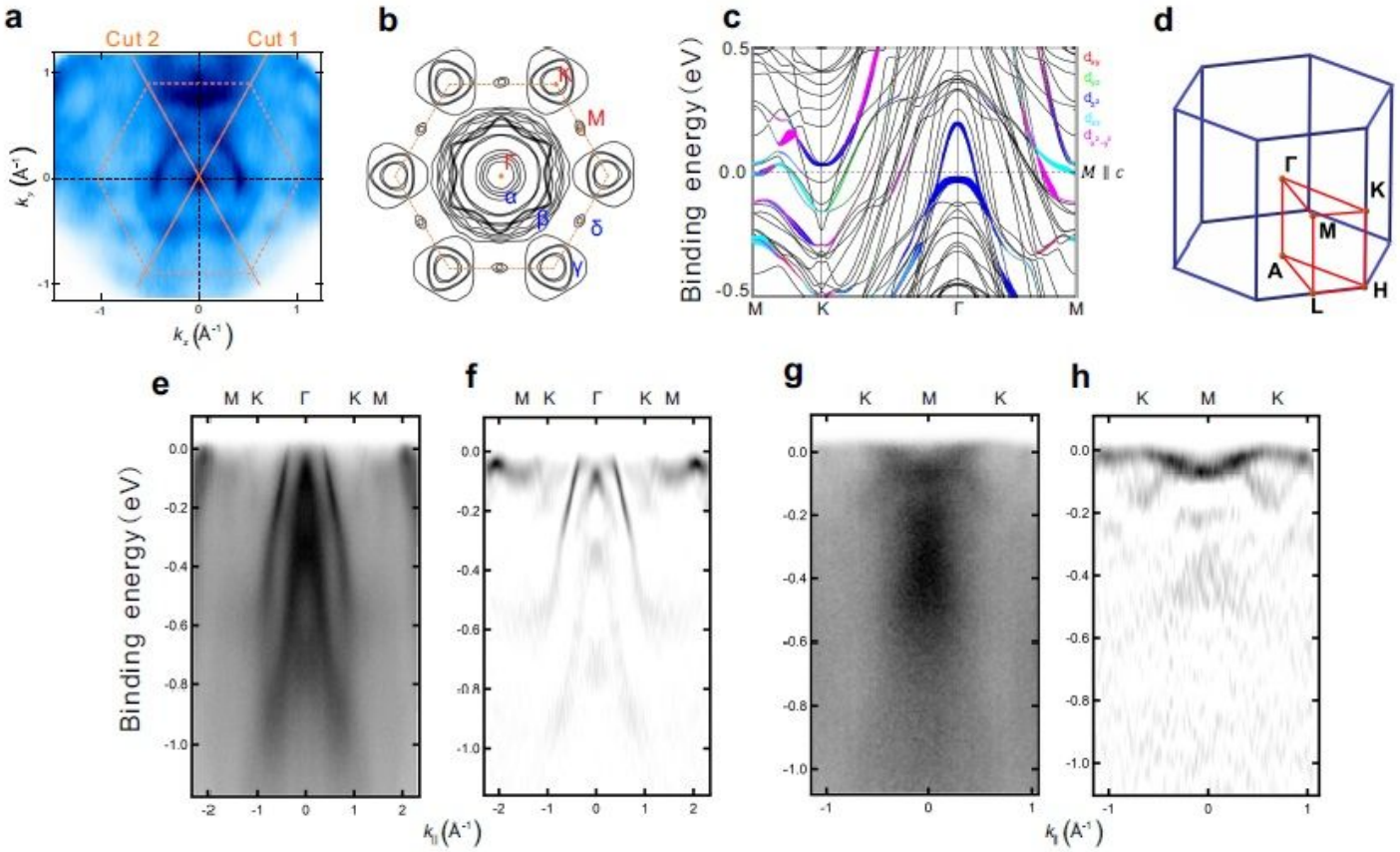

Figure 2

(see Manuscript file for figure legend)

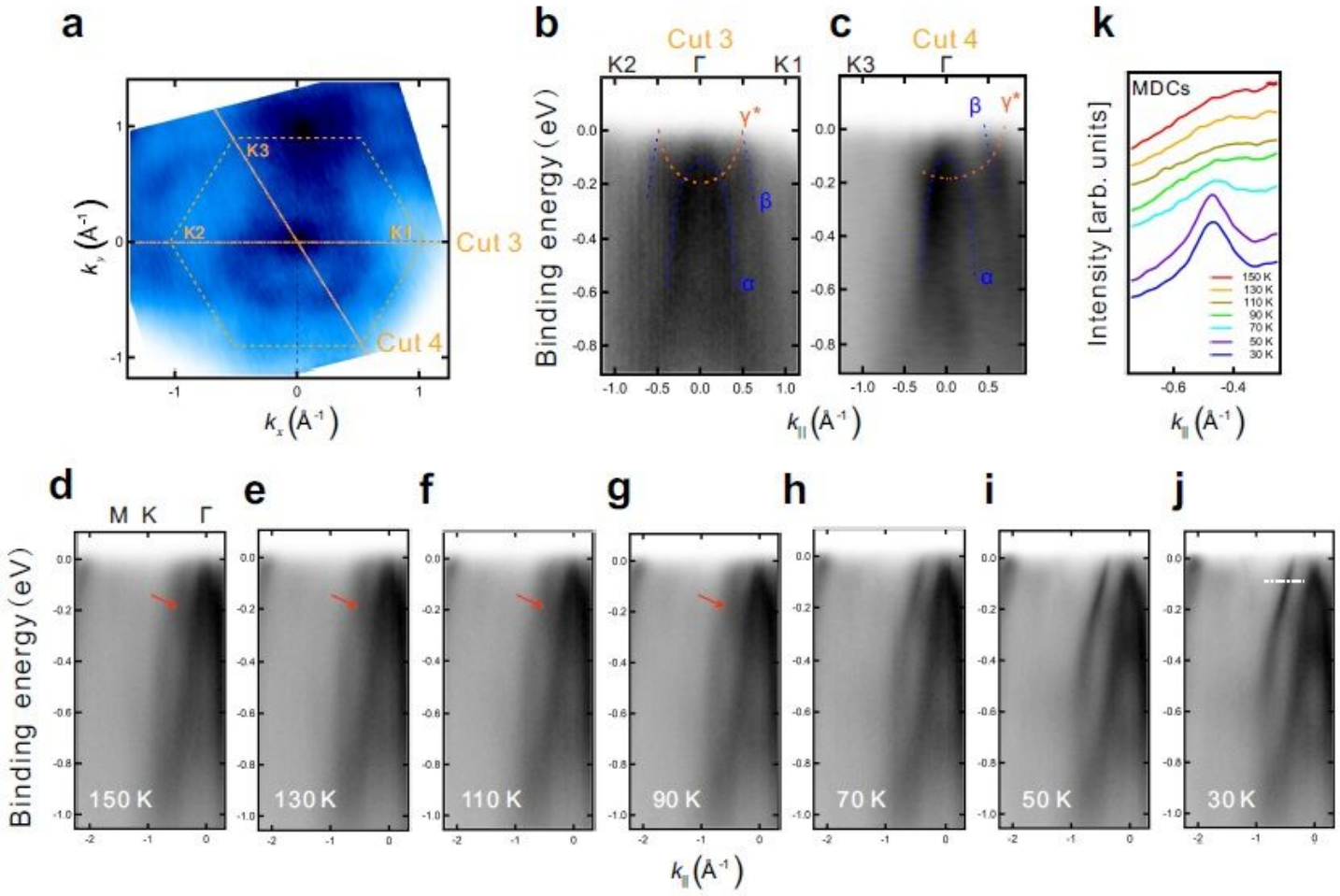

Figure 3

(see Manuscript file for figure legend)

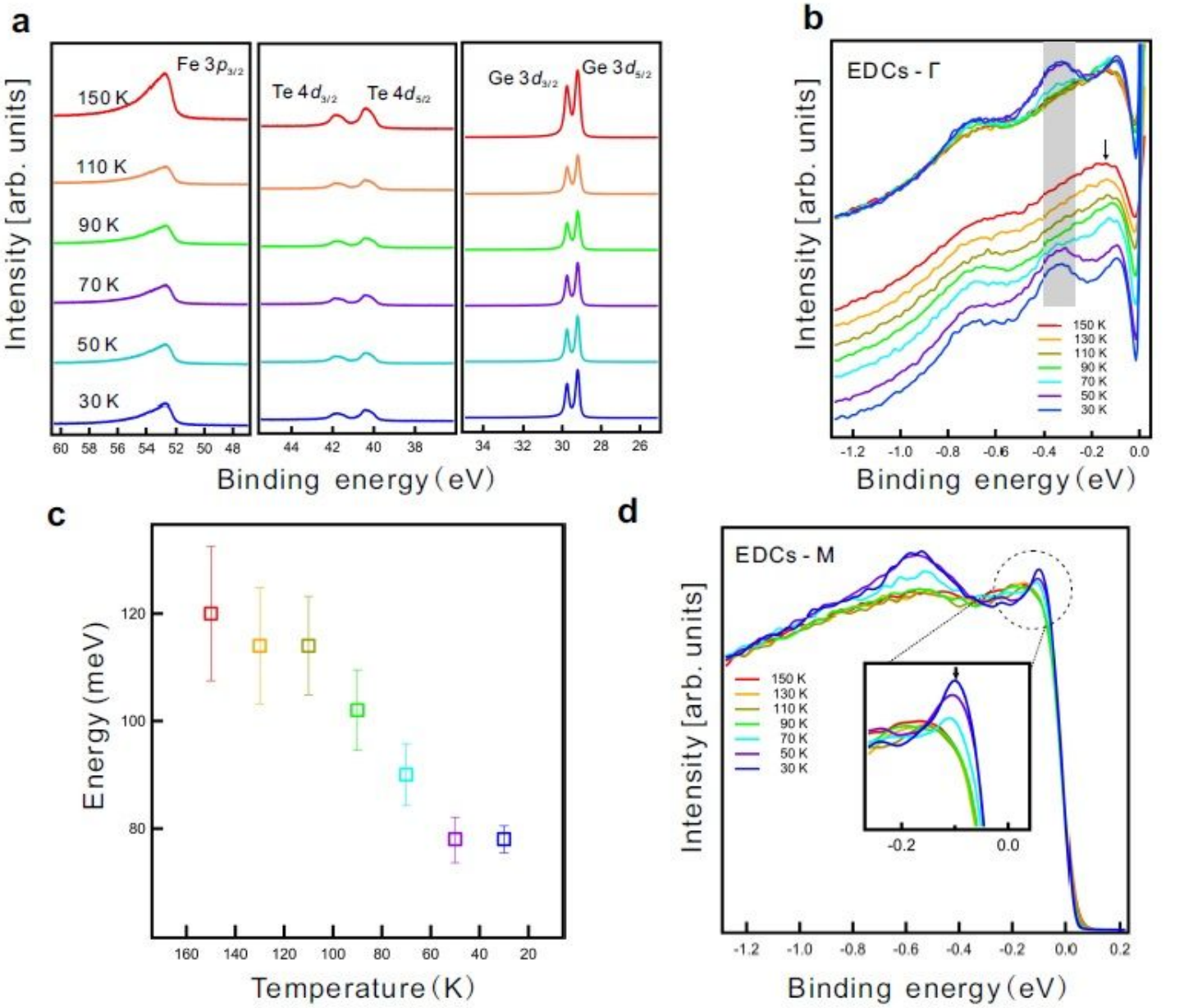

Figure 4

(see Manuscript file for figure legend)

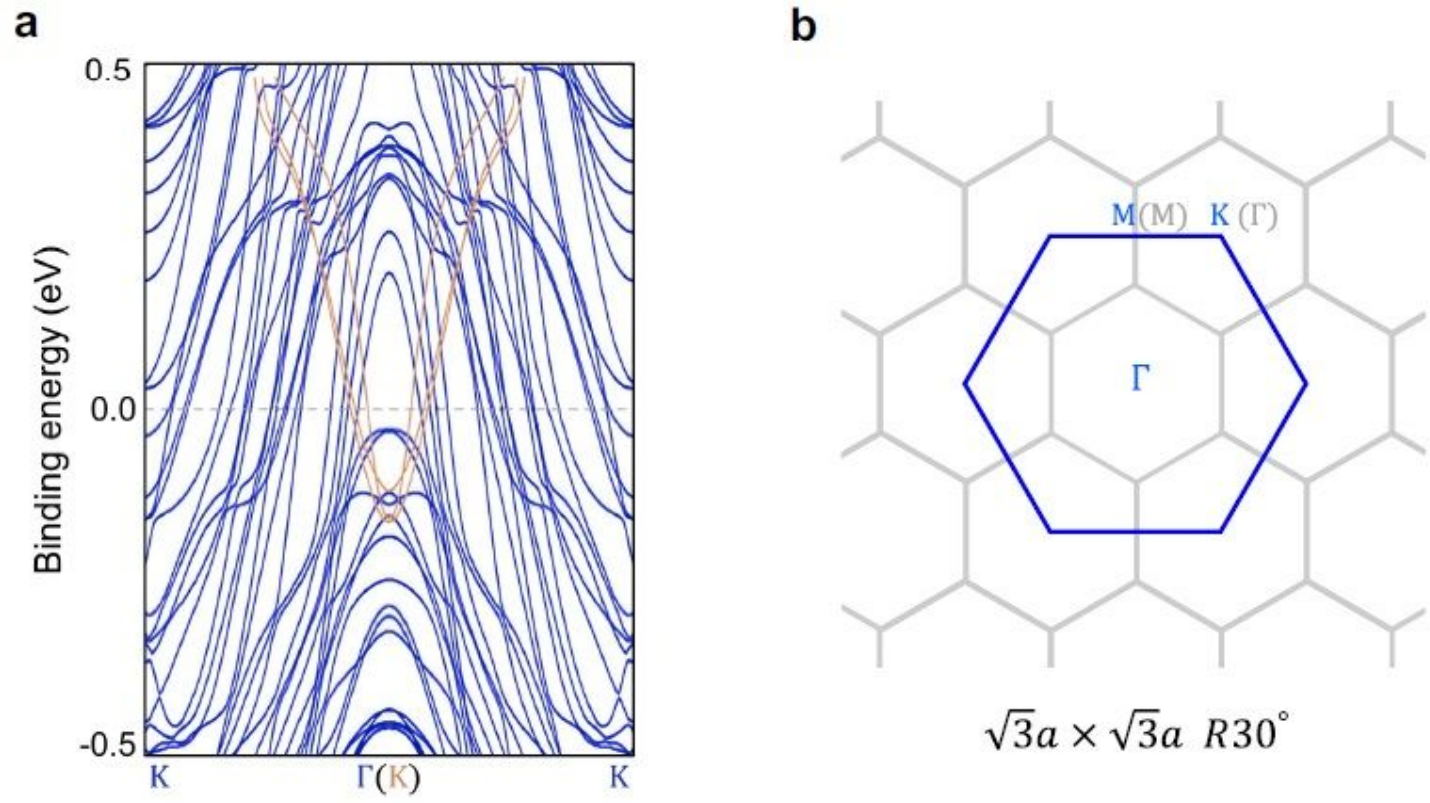

Figure 5

(see Manuscript file for figure legend)

Supplementary Files

This is a list of supplementary files associated with this preprint. Click to download.

- FGTsupplementary.pdf